

Quantum Confinement and Surface Effects on the Itinerant Ferromagnetism in Ni and Ni–Fe Nanowire Arrays: An Ab Initio Study

Ikram Ziti, Mohammed Réda Britel, Adel Bouajaj, and Chumin Wang*

Coordination number reduction of surface atoms and spatial confinement of itinerant electrons are decisive factors in the nano-ferromagnetism. Impacts of these factors on the ferromagnetic moments of Ni and Ni–Fe nanowire (NW) arrays are quantified by means of the density functional theory through both atomic-orbital and plane-wave approaches. A systematic study of the wire diameter, interwire distance and chemical composition on the magnetic properties were carried out in eight thin nanowires to investigate the limiting cases of confinement and surface effects. The results reveal a growth of the magnetic moment when the wire diameter diminishes, due to the decrease of average coordination number which reduces the 3d electronic band width and then a larger spin population contrast. This fact is consistent with experimental data obtained from Ni nanoparticles and NWs. Moreover, we found a critical interwire distance, which is the minimum separation that maintains the individual NW magnetic moment. Finally, both local and global magnetic moments of Ni–Fe NWs obtained from the ab initio calculations are compared with experimental ones and a good consistency is observed.

1. Introduction

Magnetic nanowire arrays have received considerable interest due to their applications in ultra-high density magnetic storage media, nanosensors and microwave devices.^[1–4] The physical properties of these arrays significantly differ from their corresponding bulk systems, as occurred in giant magnetic resistance^[5] and photonic band gap.^[6] In particular, nickel nanowires (Ni NWs) have become increasingly mandatory for specific applications such as sensors,^[7] solar cells,^[8] biotechnology,^[9] and microelectronics.^[10] Furthermore, Ni NWs offer the possibility to improve the magnetic recording density up to 2Tb/in²,^[11] where each nanowire records one bit of information.

Dr. I. Ziti, Prof. C. Wang
Instituto de Investigaciones en Materiales
Universidad Nacional Autónoma de México
CDMX, 04510, Mexico
E-mail: chumin@unam.mx

Dr. I. Ziti, Prof. M.R. Britel, Prof. A. Bouajaj
Laboratory of Innovative Technology
National School of Applied Sciences
Abdelmalik Essaâdi University
Tangier, Morocco

DOI: 10.1002/pssb.201700618

Consequently, there is an increasing research interest, through both theoretical and experimental investigations, to overcome this limit by reducing the wire diameter and interwire distance.^[12–16]

On the experimental side, among methods for preparing Ni NWs like nanolithography,^[17] self-assembly,^[18] sol-gel,^[19] atomic layer,^[20] and electro deposition^[21] techniques, the template-assisted method offers a highly efficient and low-cost fabrication procedure for the growth of NW arrays with high degree of NW spatial ordering.^[22] In particular, nanoporous alumina templates combined with the electrodeposition technique provide a small Ni NWs diameter reaching to 5 nm^[23] or as small as 4 nm by using carbon nanotube cavities.^[24] These nanoscale materials possess an electronic behavior qualitatively different from their bulk one, mainly due to the quantum confinement. For example, such confinement

has deep effects on the itinerant ferromagnetism, in contrast to the localized ferromagnetism occurred in rare earth metals, since the confinement of itinerant electrons in some directions could grow the band separations moving electrons from 3d to 4s band and leading to a larger magnetic moment of the nanostructure. Another related feature of nanomaterials is the very high ratio between the surface atom number and the bulk one, which could further enhance the itinerant ferromagnetism because a reduced average coordination number diminishes the 4s-band width, increases its occupation through a higher density of states, and consequently decreases the occupation of 3d bands in transition metals like Fe, Co, and Ni.^[25] Hence, the quantum confinement combined with high surface–volume atomic ratio enhance the unbalance between the spin-up and spin-down populations, which leads to an improvement of itinerant ferromagnetic moments.

From the theoretical viewpoint, there are essentially two ways for modeling the ferromagnetic properties of solids. The first one is the semi-empirical approach, which has the advantage of being simple and capable to study complex structures.^[26] However, this approach involves parameters whose variation in nanostructures is difficult to predict. In this work, we choose the second one by means of ab initio calculations, which are especially appropriate for the analysis of surface, structural order and shape effects on the NW properties. Nevertheless, this kind

of studies is very time consuming, since many electron effects are included. Particularly, the density functional theory (DFT) provides an efficient alternative to carried out ab initio studies of electronic behavior in nanostructures.^[27]

Few theoretical studies have been carried out to address the magnetic properties of NWs as a function of its interwire distance. For instance, Robles et al. studied the local magnetic moment distribution of monoatomic Co wires supported on Pd substrate for different interwire distances by means of self-consistent *spd*-tight-binding model,^[28] while the enhancement of Co NW coercivity with interwire distance for parallel applied magnetic field was analyzed by employing the Monte Carlo method.^[29] On the other hand, Kang et al. found, using DFT calculations, an optimum interwire distance which depends on the composition of $\text{Mo}_6\text{S}_{9-x}\text{I}_x$ NWs.^[30] Hence, a systematic investigation on the magnetic property variation of Ni NWs with wire diameter and interwire distance is very desirable.

On the other hand, nickel combined with iron exhibits a very high permeability and a diminishing coercive field,^[31] in comparison with traditional high-frequency ferrites. This compound has been mostly used in hard disk drive heads and high frequency magnetic devices.^[32] In particular, the invar alloy $\text{Ni}_{0.35}\text{Fe}_{0.65}$ has a low thermal expansion coefficient and is useful for precision instruments.^[31] In general, $\text{Ni}_x\text{Fe}_{1-x}$ nanowires have a higher saturation magnetization than the corresponding bulk one, whose magnitude has a decrease trend with the addition of Ni, as observed in the Slater-Pauling curve.^[33] In this study, we analyze the local and global magnetic moments of $\text{Ni}_x\text{Fe}_{1-x}$ nanowires starting from a face-centered-cubic (FCC) Ni structure. A variety of experimental studies on $\text{Ni}_x\text{Fe}_{1-x}$ NWs have been performed,^[31,34,35] while on the theoretical side there are very few ab initio studies addressing $\text{Ni}_x\text{Fe}_{1-x}$ NWs. Recently, magnetic properties of $\text{Ni}_x\text{Fe}_{1-x}$ NWs have been studied using the DFT applied to body-centered-cubic (BCC) (110)-oriented NWs.^[36]

In this article, we investigate the permanent magnetic moment of Ni and Ni-Fe NW arrays, as well as its dependence on the NW shape, diameter, interwire distance, and chemical composition, in order to analyze the confinement and surface effects on the itinerant magnetic properties. Nowadays, the DFT calculations are mainly based on plane-wave or atomic-orbital basis, and we first perform a comparative study of both approaches to address the magnetization of Ni NWs using eight different NW geometries. In the second part, we analyze the quantum confinement effects on the permanent magnetic moments (μ) obtained from the difference between integrated spin-up and spin-down densities of states, for different NW diameters, interwire distances, and Ni-Fe alloys. In fact, up to our knowledge, we are reporting for the first time an ab initio analysis of interwire distance effects on the ferromagnetic properties of Ni NW arrays. Finally, the ab initio results are compared with experimental ones and a good concordance is observed.

2. Computational Method

For ab initio calculations, the electronic wave function can be expressed as a linear combination of atomic orbitals or plane waves, where the former stresses the local environment while the latter emphasizes its delocalization nature. In fact, the electrons in

Table 1. Summary of the parameters used in DFT calculations.

	DMol ³	CASTEP
Total energy convergence tolerance	1×10^{-7} Ha/atom	5×10^{-6} eV atom ⁻¹
Maximum force convergence tolerance	3×10^{-4} Ha Å ⁻¹	0.01 eV Å ⁻¹
Maximum stress convergence tolerance		0.02 GPa
Maximum displacement convergence tolerance	5×10^{-4} Å	5×10^{-4} Å
Self-consistent field tolerance	10^{-6} (Density)	5×10^{-7} eV atom ⁻¹
k-point sample spacing (Δk)	0.04 Å ⁻¹	0.04 Å ⁻¹
Cutoff energy		1000 eV
Smearing energy	10^{-4} Ha	

solids behave neither strongly bounded around ions nor as a fully free particle. In this work, the DFT calculations were carried out by using DMol³^[37] and CASTEP^[38] codes respectively based on atomic orbitals and plane waves. Our calculations were performed at zero temperature in the DFT framework, which has been applied to the magnetic properties of clusters and NWs.^[39] In addition, we use the generalized gradient approximation (GGA) for the exchange-correlation energy calculation developed by Perdew and Wang in 1991^[40] for both atomic-orbital and plane-wave approaches, as well as an unrestricted spin polarization to quantify the magnetic moments.

For DMol³ calculations, all-electron double numerical plus polarization basis set (DNP) is selected. Such full electron calculations provide a better prediction of the total energy and magnetic moments, as well as eliminate the influence of pseudopotentials on the results. On the CASTEP side, we include an on-site electron-electron interaction U to improve the accuracy of DFT functional for the ground state of correlated electronic systems.^[41] The selected value of Hubbard U was

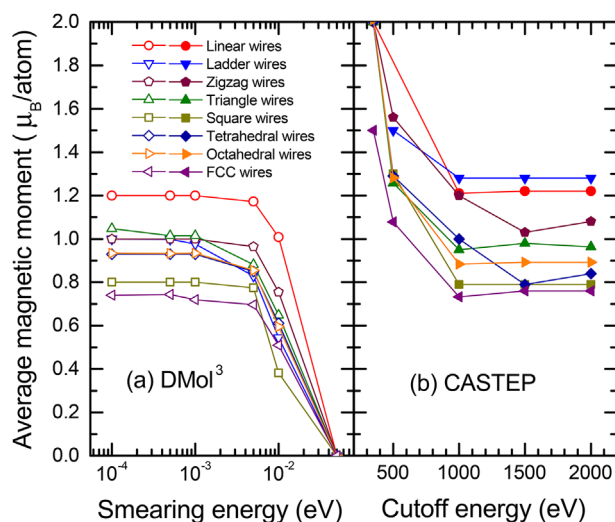
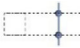

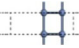

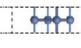





Figure 1. Average magnetic moments per atom as functions of (a) the thermal smearing energy and (b) the cutoff energy, respectively obtained from DMol³ (open symbols) and CASTEP (solid symbols) calculations for eight analyzed wires.

Table 2. Nomenclature of analyzed nanowires and some properties.

Geometry								
Name	Linear	Zigzag	Ladder	Triangle	Square	Tetrahedral	Octahedral	FCC
N	1	2	2	3	4	4	5	9
$\langle Z \rangle$	2	2	3	3.5	4	5	4.8	7.1
c (Å)	2.211	3.014	2.244	2.854	2.320	3.245	2.692	2.953

2.5 eV, since it leads to the correct magnetic moments of both Ni and Fe bulk systems. The interactions between core and valence electrons were described through norm conserving pseudopotentials. In **Table 1**, we summarize the main parameter values used in both DMol³ and CASTEP calculations, whose first six ones were taken to be equal or more stringent than the best-quality default values of each software package while the last two have been chosen after a detailed analysis of their effects on the magnetic moments.

To obtain accurate magnetic moments (μ) using minimal computing effort, we started with a detailed analysis of the DFT calculation parameters. Our calculations reveal that the most sensitive parameters of DMol³ and CASTEP are respectively the thermal smearing energy (η) and cutoff energy (E_{cut}), as shown in **Figure 1**(a) and (b) for eight types of NWs, given that the values of η and E_{cut} establish the calculation computing time and the resulting μ .

The supercell technique is used for periodic NW arrays with different atomic arrangements based on the FCC Ni structure. For this parameter analysis, we use tetragonal supercells with $a = b = 10.572$ Å in the XY plane and c depending on each analyzed NW along the z -direction, as illustrated in **Table 2**. During

the geometry optimization procedure, the supercells modify their size maintaining the right angles. It would be worth mentioning that the typical computation time of CASTEP geometry optimization with a cutoff energy of 1000 eV is about 90000 seconds, while using DMol³ this computing time reduces to about hundreds of seconds. Observe also that for both approaches the μ converges to its limiting values. For example, the μ of linear wires varies from 0.0 to $1.2 \mu_B/\text{atom}$ when $\eta \rightarrow 0$ and from 2.0 to $1.2 \mu_B/\text{atom}$ when $E_{\text{cut}} \rightarrow \infty$. In general, η establishes the full width at half maximum (FWHM) which affects the accuracy and computing time consuming of almost all spectra integrals, while E_{cut} determines the extension of wave function basis and then the size of mean-field Hamiltonian to be diagonalized in each step of the self-consistent field calculation. In addition, the results of **Figure 1** seem to show some general correlations between resulting magnetic moments and wire diameter by quantum confinement effects; such correlation will be analyzed in detail in

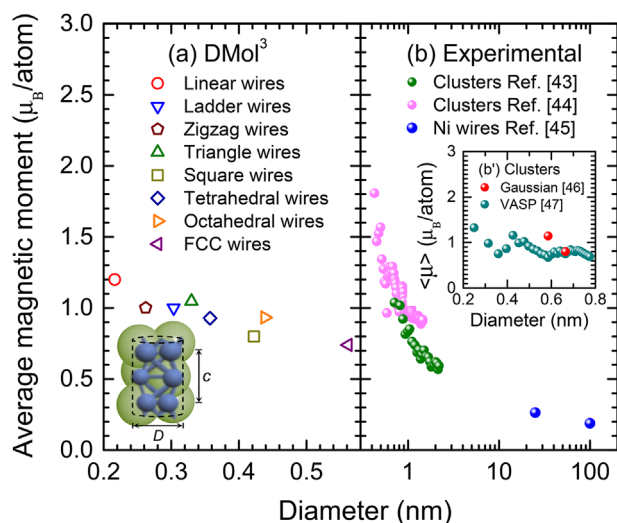


Figure 2. a) Calculated average magnetic moments as a function of the NW diameter (D) in comparison with b) experimental data of Ni clusters^[43,44] and Ni NWs.^[45] The insert of (a) presents a sketch of the cylinder model, in which the diameter D , unit cell length c and Ni ionic radii (green globes) are indicated, while (b') shows theoretical magnetic moments of Ni clusters obtained from Gaussian^[46] and VASP.^[47]

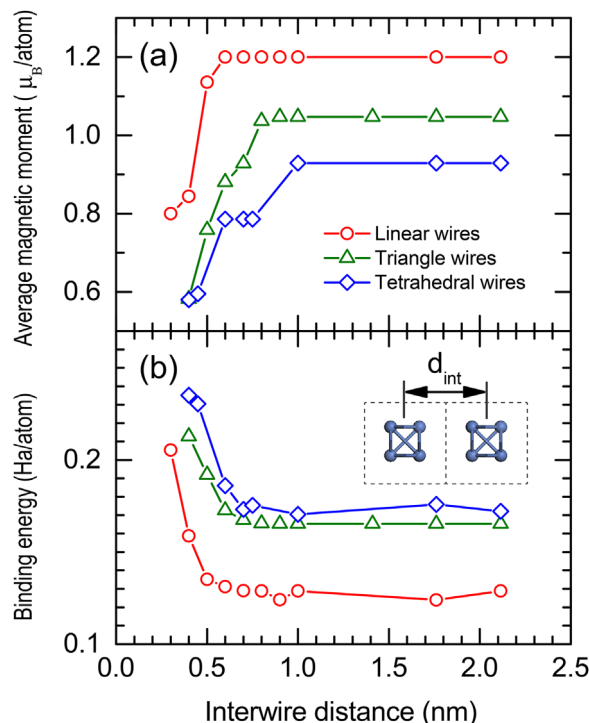


Figure 3. a) Average magnetic moment (μ) and b) binding energy, both per atom, as functions of the interwire distance (d_{int}), as illustrated in the inset of (b), for linear (red circles), triangular (green triangles), and tetrahedral (blue rhombuses) NWs.

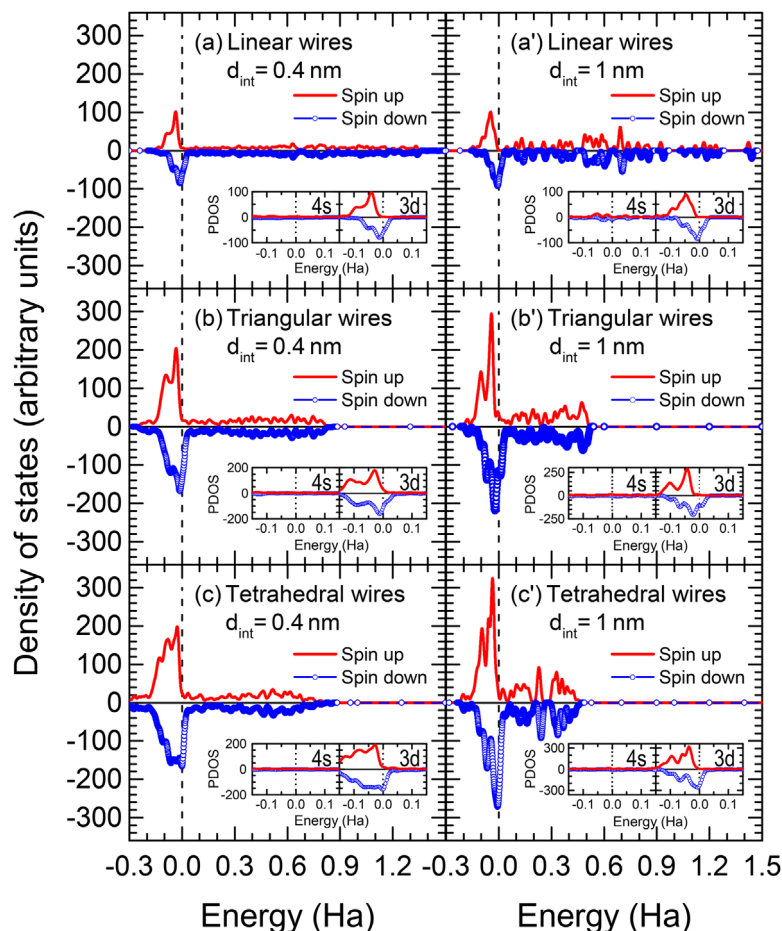


Figure 4. Electronic density of states of (a,a') linear, (b,b') triangular, and (c,c') tetrahedral nanowires with interwire distances of (a–c) 4 Å and (a'–c') 10 Å for spin-up (red curves) and spin-down (blue circles) electrons. The inserts show the partial densities of states (PDOS) for the 3d and 4s electronic bands. The dashed lines indicate the Fermi energy level.

the next section. Moreover, given that both DMol³ and CASTEP calculations provide qualitatively same results, in contrast of their dramatically different computing efforts, the rest of this study will be carried out within the DMol³ framework.

3. Results

In order to study the relationship between the NW morphology and its magnetic properties, we start from the simplest linear wire with a single atom per unit cell up to the called FCC wires containing nine atoms in each unit cell. Table 2 shows the nomenclature, number of atoms in the unit cell (N), averaged coordination number $\langle Z \rangle$, and the unit-cell z -direction length c for all studied NWs, when the interwire distance is 10 Å. It is worth mentioning that after the geometry optimization we observe a general structural contraction along the wire axes (z -direction) for all analyzed NWs, when the interwire distance is larger than 10 Å. At the same time, expansions of first-neighbor bond lengths lying on the XY plane are found for the two thickest analyzed NWs (octahedral and FCC wires), that is, from 2.492 to 2.672 Å, which joins with the structural contraction in

z -direction leading to an almost constant unit cell volume. A similar behavior of NW structural modifications during the DFT geometry optimization has been reported for Fe in Ref. [42].

To estimate the NW diameter, we started from the Ni metallic (covalent) radii of $r = 1.246$ Å and a volume of 8.103 Å³ for each Ni atom. Thus, the Ni NW diameters (D) were determined by using an infinite cylinder model, whose volume per unit cell length c is equal to the total volume of N atoms in the unit cell, that is, $\pi D^2 c / 4 = N 4 \pi r^3 / 3$. A schematic representation of this cylinder model is shown in the inset of Figure 2(a). The used values of N and c for each analyzed NW are given in Table 2. Figure 2(a) shows the obtained average magnetic moment ($\langle \mu \rangle$) as function of NW diameter (D) after the geometry optimization. This $\langle \mu \rangle$ is calculated by averaging the permanent magnetic moment of each atom in the NW, since in general the μ of surface atoms is larger than that of interior ones.

Notice a general decrease tendency of $\langle \mu \rangle$ with the growth of NW diameter in Figure 2(a), whose values are found between the Ni atomic magnetic moment of $2 \mu_B$ /atom and its bulk value of $0.6 \mu_B$ /atom. This tendency is consistent with the permanent magnetic moments measured in Ni nanoclusters^[43,44] and nanowires^[45] shown in Figure 2(b). In particular, the magnetic

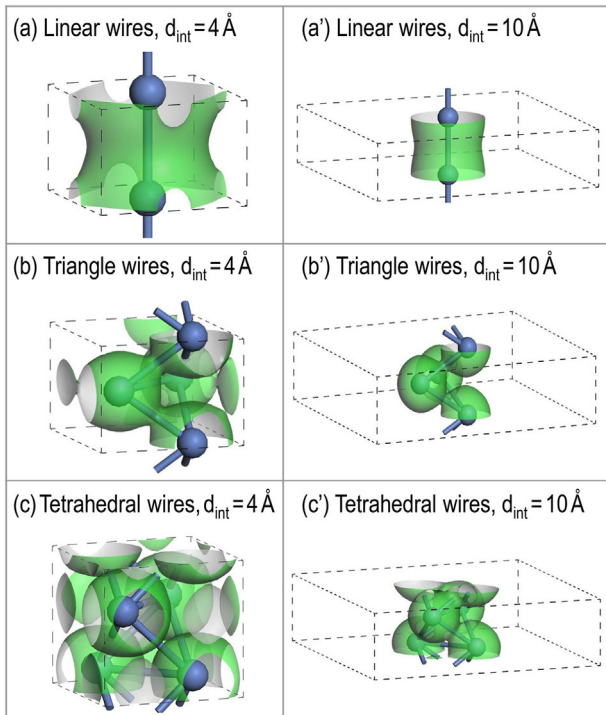


Figure 5. Electron density isosurfaces of (a,a') linear, (b,b') triangular, and (c,c') tetrahedral nanowires, respectively, for normalized total electron densities of 0.07, 0.35, and 0.3, when the interwire distance is (a-c) 4 Å and (a'-c') 10 Å.

moments of Ni nanoclusters ascend to $1.8 \mu_B/\text{atom}$, which is significantly larger than our nanowire results and could be a consequence of the three-dimensional quantum confinement in such nanoclusters. In fact, the results of Figure 2(a) obtained from NWs of infinite length establish a lower bound for the ferromagnetic moment per atom of NWs with arbitrary length, because such magnetic moment is generally enhanced by both the quantum confinement and the surface/volume ratio, or equivalently decreased with the average coordination number. The non-monotonic decrease of $\langle \mu \rangle$ in Figure 2(a) could be related to the morphological variation between analyzed NWs.

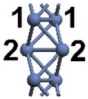
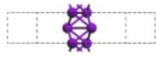
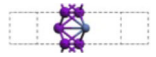
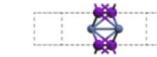
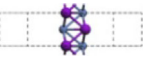
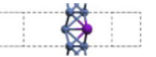
The diminution of magnetic moment with diameter observed in Figure 2 can be understood as a consequence of the quantum confinement on itinerant electrons, that is, the electronic band of 3d orbital goes to separate from that of 4s when the NW diameter reduces, which leads to a higher occupation of this 4s band and accordingly a larger magnetic moment originated from a bigger contrast between the populations of spin up and spin down 3d bands. On the other hand, the band width grows with $\langle Z \rangle$ and it leads to a larger overlap between the spin-up and spin-down sub-bands, which diminishes the sub-band occupation contrast and then a reduced magnetic moment, because the shift of one respect to the other sub-band is mainly determined by the on-site Coulombic repulsion interaction independent on $\langle Z \rangle$. Hence, for the case of NWs, the combined effect of the confinement in XY plane and surface reduction of $\langle Z \rangle$ produces a clear growth of the permanent magnetic

Table 3. Average magnetic moments^{a)} of Ni and Fe atoms in $\text{Ni}_x\text{Fe}_{1-x}$ octahedral wires^{b)}

	Fe	$\text{Ni}_{10}\text{Fe}_{90}$	$\text{Ni}_{40}\text{Fe}_{60}$	$\text{Ni}_{60}\text{Fe}_{40}$	$\text{Ni}_{90}\text{Fe}_{10}$	Ni
Fe1	2.079	2.343	2.791	2.499	2.854	2.549
Fe2	3.147	3.059	3.219	3.220	3.270	3.270
Fe3	3.147	3.059	3.123	3.150	3.206	3.237
$\langle \mu_{\text{Fe}} \rangle$	2.933	2.972	3.070	3.167	3.167	3.165
Ni1		0.603	0.594	0.665	0.650	0.723
Ni2		0.844	0.608	0.732	0.771	0.724
Ni3			0.788	0.732	0.775	0.872
$\langle \mu_{\text{Ni}} \rangle$		0.800	0.728	0.772	0.775	0.878
$\langle \mu_{\text{Ni-Fe}} \rangle$	2.933	2.538	2.133			0.933
						0.986
						0.986
						0.933

^{a)}In unit of Bohr magneton (μ_B) per atom; ^{b)} $\langle \mu_{\text{Fe}} \rangle$ and $\langle \mu_{\text{Ni}} \rangle$ were calculated from local values of Fe (purple spheres) and Ni (blue spheres) in $\text{Ni}_x\text{Fe}_{1-x}$ alloys.

Table 4. Local and global magnetic moments of $\text{Ni}_x\text{Fe}_{1-x}$ tetrahedral wires.

	Fe	$\text{Ni}_{25}\text{Fe}_{75}$	$\text{Ni}_{50}\text{Fe}_{50}$	$\text{Ni}_{75}\text{Fe}_{25}$	Ni
					
Fe1	2.936	3.140	3.243	3.115	
Fe2	2.936	3.070		3.115	3.349
$\langle \mu_{\text{Fe}} \rangle$	2.936	3.116	3.158	3.349	
Ni1				0.742	0.929
Ni2		0.740	0.899	0.742	0.929
$\langle \mu_{\text{Ni}} \rangle$		0.740	0.794	0.781	0.929
$\langle \mu_{\text{Ni-Fe}} \rangle$	2.936	2.522	1.976	1.423	0.929

moments compared with its bulk value, as revealed by ab initio and experimental results.

Another crucial parameter for magnetic properties of NW arrays is the interwire distance (d_{int}). In **Figure 3**, we present the variation of (a) average magnetic moment (μ) and (b) binding energy (E_b), both per atom, with d_{int} for linear (red circles), triangular (green triangles) and tetrahedral (blue rhombuses) NWs. This E_b is defined as $E_b = E_{\text{atom}} - E_{\text{total}}/N$, where E_{atom} is the energy of an independent atom and E_{total} is the total energy of a wire with N atoms.

Observe in **Figure 3(a)** the existence of a critical interwire distance, which separates a monotonic growth of (μ) for small d_{int} and a constant (μ) when $d_{\text{int}} \gg D$. This critical interwire distance is about three times the nanowire diameter (D), as seen in **Figure 2(a)**. In other words, the NWs behaves as independent ones when d_{int} is larger than three times D . These NWs start to feel the neighboring ones when they approach to each other, as confirmed by the binding energy of **Figure 3(b)**, whose value grows with the average coordination number ($\langle Z \rangle$). At the other limit, when the NWs are close enough, their (μ) lead to its bulk value of $0.6 \mu_B/\text{atom}$.

In **Figure 4**, spin-up (red lines) and spin-down (blue circles) densities of states (DOS) are shown for (a,a') linear, (b,b') triangular and (c,c') tetrahedral wires, when the interwire distance d_{int} is (a-c) 4 Å and (a'-c') 10 Å. The partial DOS for 3d and 4s electronic bands are illustrated in the insets of **Figure 4**. The Fermi energy (E_F) is indicated by dashed lines. Notice the sharp peaks in DOS for $d_{\text{int}} = 1\text{nm}$, due to their lower ($\langle Z \rangle$) than those of $d_{\text{int}} = 0.4\text{nm}$. Also, the high-density bands, located just below E_F , correspond to 3d ones and their widths grow when d_{int} diminishes, as shown in the insets of **Figure 4**. This 3d-band width growth produces a magnetic moment drop.

Likewise, we illustrate in **Figure 5** the normalized total electron density isosurfaces at 0.07, 0.35 and 0.3 respectively for (a,a') linear, (b,b') triangular and (c,c') tetrahedral wires with the interwire distance (d_{int}) of (a-c) 4 Å and (a'-c') 10 Å. Observe the electron density overlaps, appeared as holes on the isosurfaces, between atoms of neighbor wires when $d_{\text{int}} = 4\text{Å}$, which confirms the increase of coordination number when the NWs approach. Moreover, note the disconnection of internal

electronic isosurfaces in **Figure 5(c)** compared with **Figure 5(c')**, when its surface atoms are bound to those of neighbor NWs.

We further study the local and global magnetic moments (μ) of $\text{Ni}_x\text{Fe}_{1-x}$ with $0 \leq x \leq 1$ for octahedral and tetrahedral NWs obtained by DMol³ calculations, as respectively shown in **Tables 3 and 4**. There are several non-equivalent structural configurations for each compound and the global $\langle \mu_{\text{Ni-Fe}} \rangle = x \langle \mu_{\text{Ni}} \rangle + (1-x) \langle \mu_{\text{Fe}} \rangle$ is calculated over all the possible configurations with the same probability. For example, the unit cell of $\text{Ni}_{20}\text{Fe}_{80}$ octahedral NW has five configurations and only two of them are non-equivalents. Note the dependence of local μ on its environment surrounding by Fe (purple large spheres) or Ni (blue small spheres) atoms. For instance, in **Table 3** the magnetic moment of atom 1 is smaller than that of the same atom at other positions, due to its higher coordination number. In **Table 4**, observe the structural contraction along the NW axes with the growth of Fe atom content. Specifically, the horizontal and diagonal interatomic distances are 2.675 and 2.383 Å in pure Fe tetrahedral wires, in comparison with 2.447 and 2.372 Å for the pure Ni case, both obtained from the DMol³ geometrical optimization process with a uniform initial Ni-bulk interatomic distance of 2.492 Å.

The average local and global magnetic moments of **Tables 3 and 4** are plotted in **Figure 6** for (a) Fe and (b) Ni atoms, as well as (c) Ni-Fe compounds versus Ni concentration x in octahedral (red solid triangles) and tetrahedral (blue solid rhombuses) $\text{Ni}_x\text{Fe}_{1-x}$ NWs, in comparison with the bulk and NW experimental data.^[31,35,48,49] The theoretical error bars in **Figure 6** (a,b) indicate the fluctuation of local μ , while the experimental ones were obtained from the corresponding references. Notice the increase of $\langle \mu_{\text{Fe}} \rangle$ with x in **Figure 6(a)**, which can be understood by considering the relative isolation of Fe atom by Ni ones. This feature is consistent with both bulk and NW experimental results. In contrast, we observe in **Figure 6(b)** an oscillating behavior of $\langle \mu_{\text{Ni}} \rangle$ and a higher value around $0.93 \mu_B$ per atom for both pure Ni octahedral and tetrahedral NWs. These facts are compared with experimental data, which show a decrease tendency with x in accordance with the explained isolating model.

In **Figure 6(c)**, note the diminution of average global magnetic moments ($\langle \mu_{\text{Ni-Fe}} \rangle$) with Ni concentration for both octahedral

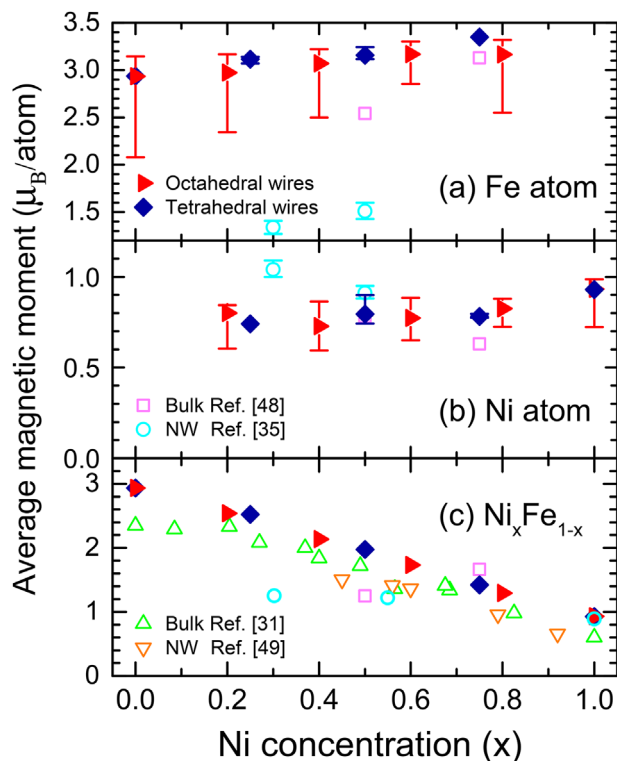


Figure 6. Local and global average magnetic moments of (a) Fe atom, (b) Ni atom and (c) Ni–Fe compound as functions of nickel concentration (x) in $\text{Ni}_x\text{Fe}_{1-x}$ nanowires, for octahedral (red solid triangles) and tetrahedral (blue solid rhombuses) wires, in comparison with bulk (magenta open squares and green open up-triangles) and NW (cyan open circles and orange open down-triangles) experimental data.

and tetrahedral NWs, which is in good agreement with bulk and NW experimental data. Moreover, there is an excellent coincidence between the theory and experiment for $\langle \mu_{\text{Ni-Fe}} \rangle$ of pure Ni NWs with $x = 1$, whose value is larger than the measured bulk one. This coincidence could be related to the fact that these two analyzed octahedral and tetrahedral NWs are directly derived from the Ni bulk FCC structure, which may not be a proper starting point for other $\text{Ni}_x\text{Fe}_{1-x}$ NWs with $x \neq 1$, since the BCC derived NWs should be more appropriate for $x \approx 0$, as done in Ref. [36] whose results are slightly smaller than those of Figure 6(c) since their NW diameter is larger than ours.

4. Conclusions

In this work we have performed a detailed ab initio study of the quantum confinement and surface effects on the itinerant ferromagnetic properties of Ni and Ni–Fe nanowires (NW). We started from an analysis of possible approaches within the DFT formalism and we chose two of them that use the plane-wave and atomic-orbital basis, respectively through CASTEP and DMol³ codes. Inside these two codes we found two sensitive parameters, the cutoff energy in CASTEP and the smearing energy in DMol³, that significantly affect both computing cost and magnetization results. Moreover, we found a critical value

for each of these two parameters and beyond these critical values both approaches predict almost the same permanent magnetic moments of eight analyzed Ni nanowires, except that the computing time of DMol³ code is considerably lower than that of CASTEP.

We further study the effects of wire diameter (D) on the magnetic moment (μ), finding a clear decay of μ with D , in accordance with experimental data of both nanoparticles and nanowires. This decay can be explained by the quantum confinement scene, in which the 3d electronic band separates from 4s one making a higher occupation in the latter and then a larger μ originated from a bigger contrast between the spin-up and spin-down 3d band populations. In the absence of such confinement we recuperate its limiting bulk value of $0.6 \mu_B/\text{atom}$

Regarding to the importance of interwire distance (d_{int}) on the μ of NW arrays, we found a critical d_{int} for each of the three analyzed NWs, which separates a constant behavior of μ from an almost linear decreasing one. This phenomenon can be understood from the growth of average coordination number ($\langle Z \rangle$) when d_{int} diminishes, which leads to a larger width of electronic bands and then a larger overlap between the spin-up and spin-down sub-bands producing a smaller μ , since the shift of these two sub-bands is mainly determined by the on-site Coulombic repulsion interaction independent on $\langle Z \rangle$. This explanation scheme was confirmed by the results of spin-up and spin-down density of states shown in Figure 4, as well as electronic density isosurfaces illustrated in Figure 5.

For $\text{Ni}_x\text{Fe}_{1-x}$ alloys, we have investigated the local μ of Fe and Ni atoms as well as the global one in Ni–Fe NWs. The results show a remarkably higher local μ of Fe than that of Ni atom, remaining both almost constant values regardless the Ni concentration x , as well as a notable variation of this local μ at structurally non-equivalent sites. In consequence, the global μ obtained from the average over all possible configurations presents a monotonic decay with x confirming the experimental behaviors obtained from bulk and NW measurements. Also, we found an additional structural contraction along the NW axis, beside that occurred in pure Ni NWs, when Ni atoms are gradually substituted by Fe ones.

In summary, this article attempts to contribute a deeper understanding of the itinerant ferromagnetism at nanoscale. Our ab initio results reveal that the increase of μ due to the reduction of D and/or enlargement of d_{int} are consequences of the quantum confinement and reduced coordination number at surface. Moreover, this ab initio study confirms the suitability of DFT atomic-orbital approach for the investigation of itinerant 3d ferromagnetic properties, predicting their general features and behaviors. To accurately reproduce the experimental data, a DFT with adjustable-parameter hybrid functionals would be required. On the other hand, the critical d_{int} found in this article establishes a theoretical limit for the design of magnetic recording devices with extreme high density. Such critical d_{int} can be achieved by adding surfactant agents to avoid the agglomeration of NWs.^[50] This work can be extended to analyze other itinerant magnetic NWs with larger D at finite temperature by integrating spin-up and spin-down DOS (see Figure 4) weighted by the Fermi-Dirac distribution function. The study of $\text{Ni}_x\text{Fe}_{1-x}$ NWs can be also carried out starting from a BCC

structured NW, as used in Ref. [36]. These extensions are currently in progress.

Acknowledgements

We would like to thank Alessio Palavicini, Alberto López, Alejandro Pompa and Cain González for their technical assistance. This work has been partially supported by Consejo Nacional de Ciencia y Tecnología of Mexico project 252943 and UNAM-DGAPA-PAPIIT project IN116317. Computations were performed at Miztli of DGTIC-UNAM.

Conflict of Interest

The authors declare no conflict of interest.

Keywords

density functional theory, magnetic moments, nickel nanowires

Received: November 12, 2017

Revised: February 1, 2018

Published online: March 22, 2018

- [1] K. Nielsch, R. B. Wehrspohn, J. Barthel, J. Kirschner, S. F. Fischer, H. Kronmüller, T. Schweinböck, D. Weiss, U. Gösele, *J. Magn. Magn. Mater.* **2002**, *249*, 234.
- [2] S. S. P. Parkin, M. Hayashi, L. Thomas, *Science* **2008**, *320*, 190.
- [3] P. D. McGary, L. Tan, J. Zou, B. J. H. Stadler, P. R. Downey, A. B. Flatau, *J. Appl. Phys.* **2006**, *99*, 08B310.
- [4] B. K. Kuanr, V. Veerakumar, R. Marson, S. R. Mishra, R. E. Camley, Z. Celinski, *Appl. Phys. Lett.* **2009**, *94*, 202505.
- [5] T. Kim, R. V. Chamrerlin, J. P. Bird, *Nano Lett.* **2013**, *13*, 1106.
- [6] L. Chen, E. Towe, *Appl. Phys. Lett.* **2005**, *87*, 103111.
- [7] M. García, A. Escarpa, *Biosens. Bioelectron.* **2011**, *26*, 2527.
- [8] I. E. Stewart, A. R. Rathmell, L. Yan, S. Ye, P. F. Flowers, W. You, B. J. Wiley, *Nanoscale* **2014**, *6*, 5980.
- [9] A. Hultgren, M. Tanase, C. S. Chen, G. J. Meyer, D. H. Reich, *J. Appl. Phys.* **2003**, *93*, 7554.
- [10] N. Vassal, E. Salmon, J.-F. Fauvarque, *J. Electrochem. Soc.* **1990**, *146*, 20.
- [11] A. S. Samardak, E. V. Sukovatitsina, A. V. Ognev, L. A. Chebotkevich, R. Mahmoodi, S. M. Peighambari, M. G. Hosseini, F. Nasirpour, *J. Phys.: Conf. Ser.* **2012**, *345*, 012011.
- [12] A. Cortés, G. Riveros, J. L. Palma, J. C. Denardin, R. E. Marotti, E. A. Dalchiale, H. Gómez, *J. Nanosci. Nanotechnol.* **2009**, *9*, 1992.
- [13] M. Motoyama, Y. Fukunaka, T. Sakka, Y. H. Ogata, S. Kikuchi, *J. Electroanal. Chem.* **2005**, *584*, 84.
- [14] T. Thurn-Albercht, J. Schotter, G. A. Kästle, N. Emley, T. Shibauchi, L. Krusin-Elbaum, K. Guarini, C. T. Black, M. T. Tuominen, T. P. Russell, *Science* **2000**, *290*, 2126.
- [15] M. Zelený, M. Šob, J. Hafner, *Phys. Rev. B* **2009**, *79*, 134421.
- [16] F. Muñoz, A. H. Romero, J. Mejía-López, J. L. Morán-López, *J. Nanopart. Res.* **2013**, *15*, 1524.
- [17] D. A. Bizyaev, A. A. Bukharaev, D. V. Lebedev, N. I. Nurgazizov, T. F. Khanipov, *Tech. Phys. Lett.* **2012**, *38*, 645.
- [18] D. Wang, D. Sun, H. Yu, Z. Qui, H. Meng, *Mater. Chem. Phys.* **2009**, *113*, 227.
- [19] B. F. Jia, L. Zhang, X. Shang, Y. Yang, *Adv. Mater.* **2008**, *20*, 1050.
- [20] S. W. Ryu, J. Yoon, H. Moon, B. Shong, H. Kim, H. Lee, *Nanotechnology* **2017**, *28*, 115301.
- [21] K. Nielsch, F. Müller, A. Li, U. Gösele, *Adv. Mater.* **2000**, *12*, 582.
- [22] M. Vázquez, M. Hernández-Vélez, K. Pirola, A. Asenjo, D. Navas, J. Velázquez, P. Vargas, C. Ramos, *Eur. Phys. J. B* **2004**, *40*, 489.
- [23] M. Kröll, W. J. Blau, D. Grandjean, R. E. Benfield, F. Luis, P. M. Paulus, L. J. de Jongh, *J. Magn. Magn. Mater.* **2002**, *249*, 241.
- [24] B. K. Pradhan, T. Kyotani, A. Tomita, *Chem. Commun.* **1999**, 1999, 1317.
- [25] D. A. Papaconstantopoulos, *Handbook of the Band Structure of Elemental Solids*, 2nd edn, Springer, New York, USA **2015**, pp. 172–176.
- [26] P. Alfaro, R. Cisneros, M. Bizarro, M. Cruz-Irisson, C. Wang, *Nanoscale* **2011**, *3*, 1246.
- [27] Y. Bonder, C. Wang, *J. Appl. Phys.* **2006**, *100*, 044319.
- [28] R. Robles, J. Izquierdo, A. Vega, *Phys. Rev. B* **2000**, *61*, 6848.
- [29] K. Zhong, Z. Huang, Z. Chen, Q. Feng, Y. Yang, *Trans. Nonferrous Met. Soc. China* **2008**, *18*, 700.
- [30] S. Kang, Y. Kwon, D. Tománek, *Phys. Rev. B* **2010**, *82*, 205427.
- [31] B. Glaubitz, S. Buschhorn, F. Brüßing, R. Abrudan, H. Zabel, *J. Phys.: Condens. Matter* **2011**, *23*, 254210.
- [32] J.-G. Zhu, *Mater. Today* **2003**, 22.
- [33] Y. Kakehashi, O. Hosohata, *J. Phys.* **1988**, *49*, 73.
- [34] M. Salem, P. Sergelius, R. Zierold, J. Moreno, D. Görlitz, K. Nielsch, *J. Mater. Chem.* **2012**, *22*, 8549.
- [35] S. Chang, C. Yang, H. Ma, Y. Tseng, *J. Magn. Magn. Mater.* **2013**, *332*, 21.
- [36] S. A. Aravindh, S. M. Jaya, M. C. Valsakumar, C. S. Sundar, *Appl. Nanosci.* **2012**, *2*, 409.
- [37] a) B. Delley, *J. Chem. Phys.* **2000**, *113*, 7756; b) B. Delley, *J. Chem. Phys.* **1990**, *92*, 508.
- [38] S. J. Clark, M. Segall, C. Pickard, P. Hasbip, M. Probert, K. Refson, M. Payne, *Z. Kristallogr.* **2005**, *220*, 567.
- [39] X. Zhang, J. Wang, Y. Gao, X. C. Zeng, *ACS Nano* **2009**, *3*, 537.
- [40] J. P. Perdew, Y. Wang, *Phys. Rev. B* **1992**, *45*, 13244.
- [41] V. I. Anisimov, O. Gunnarsson, *Phys. Rev. B* **1991**, *43*, 7570.
- [42] C. Jo, J. I. Lee, *Phys. Status Solidi B* **2004**, *241*, 1427.
- [43] S. E. Apsel, J. W. Emmert, J. Deng, L. A. Bloomfield, *Phys. Rev. Lett.* **1996**, *76*, 1441.
- [44] I. M. L. Billas, A. Chatelain, W. A. Heer, *Science* **1994**, *265*, 1682.
- [45] S. Karim, K. Maaz, *Mater. Chem. Phys.* **2011**, *130*, 1103.
- [46] K. Lee, J. Callaway, K. Kwong, R. Tang, A. Ziegler, *Phys. Rev. B* **1985**, *31*, 1796.
- [47] W. Song, W.-C. Lu, C. Z. Wang, K. M. Ho, *Comput. Theor. Chem.* **2011**, *978*, 41.
- [48] J. W. Cable, E. O. Wollan, *Phys. Rev. B* **1973**, *7*, 2005.
- [49] O. Dragos, H. Chiriac, N. Lupu, M. Grigoras, I. Tabakovic, *J. Electrochem. Soc.* **2016**, *163*, D83.
- [50] L. Sun, Q. Chen, *Eur. J. Inorg. Chem.* **2009**, 2009, 435.